Use of a passive reaction wheel jitter isolation system to meet the Advanced X-ray Astrophysics Facility imaging performance requirements

Karl J. Pendergast, Christopher J. Schauwecker

TRW Inc., One Space Park, Redondo Beach, CA 90278

ABSTRACT

Third in the series of NASA great observatories, the Advanced X-Ray Astrophysics Facility (AXAF) is scheduled for launch from the Space Shuttle in November of 1998. Following in the path of the Hubble Space Telescope and the Compton Gamma Ray Observatory, this observatory will image light at X-ray wavelengths, facilitating the detailed study of such phenomena as supernovae and quasars. The AXAF project is sponsored by the Marshall Space Flight Center in Huntsville, Alabama.

Because of exacting requirements on the performance of the AXAF optical system, it was necessary to reduce the transmission of reaction wheel jitter disturbances to the observatory. This reduction was accomplished via use of a passive mechanical isolation system to interface the reaction wheels with the spacecraft central structure.

In addition to presenting a description of the spacecraft, the isolation system, and the key image quality requirement flowdown, this paper details the analyses performed in support of system-level imaging performance requirement verification. These analyses include the identification of system-level requirement suballocations, quantification of imaging and pointing performance, and formulation of unit-level isolation system transmissibility requirements.

Given in comparison to the non-isolated system imaging performance, the results of these analyses clearly illustrate the effectiveness of an innovative reaction wheel passive isolation system.

1.0 INTRODUCTION

In order to image light at X-ray wavelengths, the AXAF observatory will be equipped with a Wolter type I grazing incidence optical package built by Eastman Kodak under subcontract from TRW. Upon examination of figure 1, it can be seen that this package contains two sets of four nested nearly cylindrical mirrors serially located along the optical axis of the telescope. Because of the shallow incident angles and sizable focal length (approximately 10m) inherent with this type of telescope, small dynamic perturbations of the mirror surfaces due to internally generated high frequency disturbances can have significant effects in terms of image quality degradation.

Having been identified as the only significant on-orbit source of high-frequency dynamic input to the AXAF structure, reaction wheel assembly (RWA) jitter disturbances were the focus of a preliminary analysis conducted for the purpose of quantifying system imaging performance. Because this analysis indicated that the level of image quality degradation was unacceptable in comparison the appropriate system requirements, it became necessary to isolate the RWAs from the spacecraft central structure. This paper documents the various analyses performed in support of the mechanical isolation system design undertaken in response to this necessity. The end result of that effort is shown to be a sufficient reduction in transmitted RWA disturbances such that the expected X-ray image quality meets all system-level performance requirements.

The organization of the paper is as follows. A brief description of the spacecraft configuration and final isolation system design is followed by a summary of the process used to flow top-level image quality requirements down to unit-level requirements for the isolation system. The latter two sections contain a detailed description of the analytical methodology used to quantify the image quality with respect to the appropriate system-level requirements given the design of the disturbance isolators.

2.0 SPACECRAFT CONFIGURATION

Figure 2 provides an exploded view of the AXAF observatory, illustrating components important to the generation and transmission of spacecraft jitter and resultant X-ray image quality degradation. The high resolution mirror assembly (HRMA) containing four nested pairs of grazing incidence optics was produced by Hughes Danbury Optical Systems and possesses a surface integrity previously unachieved. These optical elements are held in place by a support structure assembly (SSA) that is rigidly attached to the Eastman-Kodak Corp. (EKC) telescope forward bulkhead by means of three bipod struts (set #1). This arrangement allows for a stable optical relationship between the grazing optics and the science instrument detectors located at the focal plane near the telescope aft bulkhead. The focal plane science instruments (FPSIs) are part of the Integrated Science Instrument Module (ISIM) produced by Ball Aerospace corporation that is rigidly attached to the telescope aft bulkhead. The spacecraft bus, built by TRW, surrounds the SSA, but is not directly attached to the SSA. Instead, the spacecraft bus central cylinder is rigidly attached to the telescope forward bulkhead via three additional bipod struts (set #2). Lastly, the bus design incorporates a constellation of six RWAs mounted to the bus via the specially designed reaction wheel isolator assemblies

Further author information:
KJP: Email: penderkj@elrond.sp.trw.com; Telephone: 310-813-3534
CJS: Email: chris.schauwecker@trw.com; Telephone: 310-814-6302

reaction wheel isolator assemblies (RWIAs), the design of which is the subject of this paper. This configuration yields the following path for transmission of RWA dynamic disturbances to the HRMA:

RWA (disturbance source)
→ Reaction Wheel Isolator Assembly
→ Spacecraft Central Cylinder
→ Bipod Strut Set #2
→ Telescope Forward Bulkhead
→ Bipod strut Set #1
→ SSA
→ HRMA optical elements

The transmission of dynamic disturbances from the six RWAs located around the diameter of the central cylinder cause relative rigid body jitter of HRMA optical elements as well as local deformations of the optical surfaces themselves. Both of these effects contribute to overall degradation of X-ray image resolution at the telescope focal plane, causing the image size to grow from an idealized point image. Section 4 addresses in detail the traceability of the allowable image size growth requirement from the top-level system requirements to the unit-level disturbance transmissibility requirement contained in the RWIA equipment specification. Before proceeding with that discussion, however, a description of the RWIA design and functionality is given in section 3.
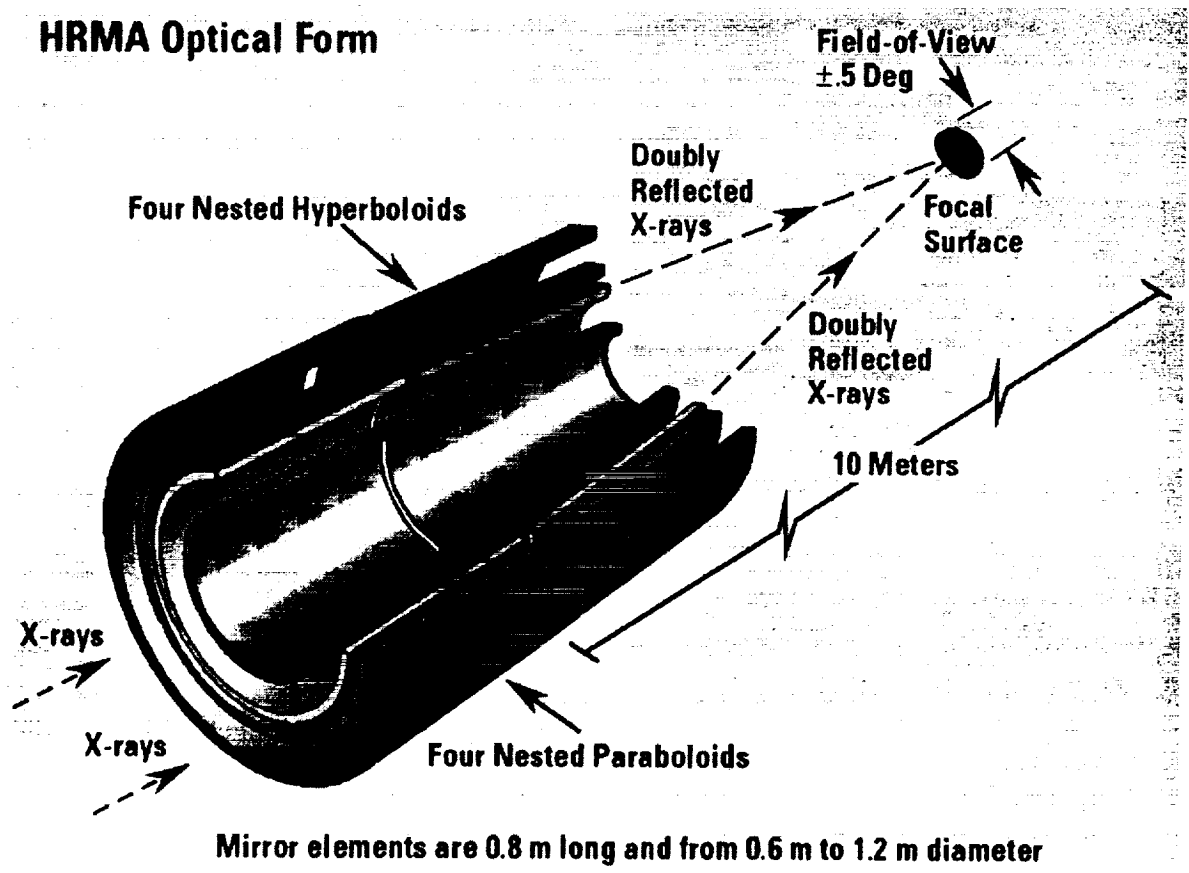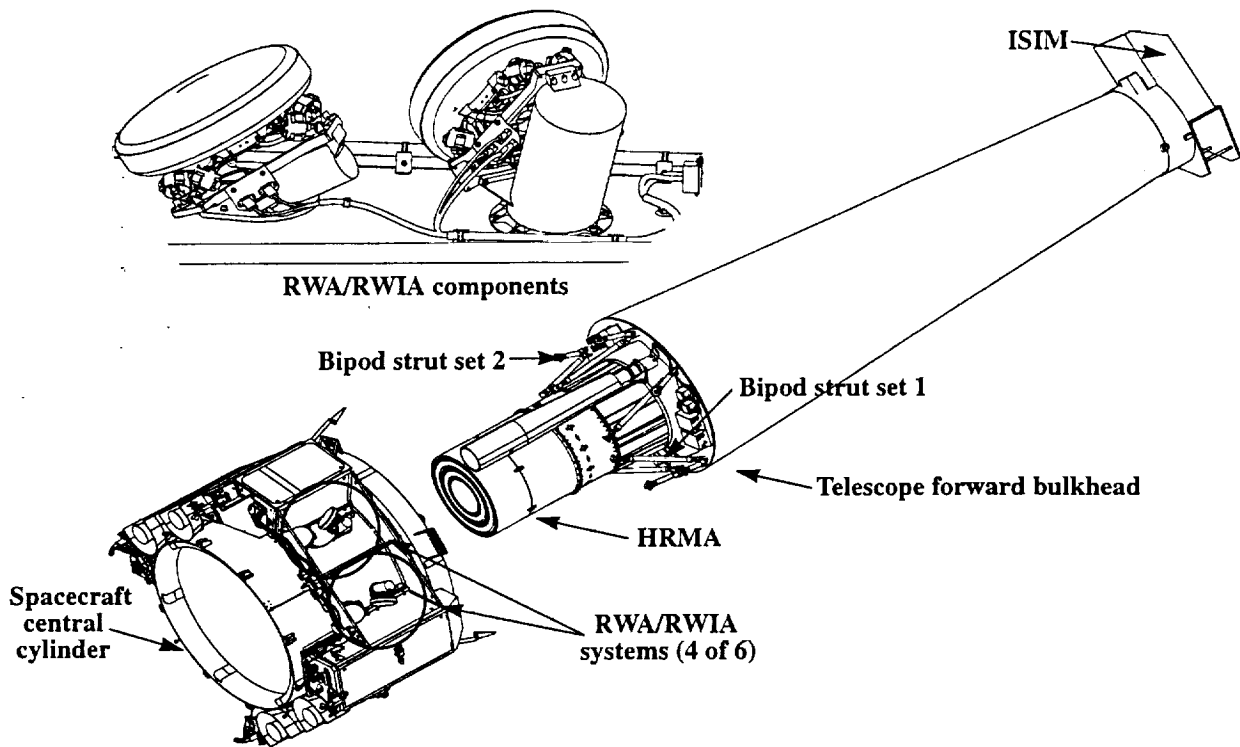

Figure 1: AXAF HRMA Optical surface configuration

Figure 2: Exploded view of the AXAF system with the RWA/RWIA components

3.0 RWIA DESIGN

The RWIA components reduce the level of RWA dynamic disturbances transmitted to the AXAF optical train via a passive mechanical design that interfaces the RWAs with the spacecraft central cylinder. The key component of the RWIA (figures 2 through 5) design is the set of six machined spring elements that utilize a bonded viscoelastic material (VEM) to provide damping. As shown in the photographs of figures 3 and 5, these spring elements serve as the interface between two larger brackets. The upper bracket, or cradle, attaches to the reaction wheel, while the lower bracket interfaces with the central cylinder of the spacecraft. Aligned in a geometry commonly known as a Stewart platform arrangement, the six springs essentially function as a truss system, with the RWA disturbance loads being transmitted to the spacecraft as axial tension/compression spring forces. The attachment points of the springs to the brackets are designed so that each spring acts as a two force member. Transverse bending effects in the springs are small and are alleviated via internal flexures coaxially aligned with the two attachment ends. Consequently, the assembly behaves approximately as a statically determinant kinematic mount. The line of action for each pair of springs intersects at the plane that contains the isolated mass center and, therefore, results in a decoupling of all fundamental modes of the combined assembly except the torsional bending mode. The angular orientation of the springs with respect to the cradle and bottom bracket is selected such that the three translational and two rocking mode frequencies are equalized. The effective axial stiffness of the springs determines the fundamental frequency of the isolator assembly. The AXAF RWIA axial stiffness was designed to meet an analytical 9 Hz cutoff frequency followed by a -12 dB/octave rolloff, and was chosen to correspond with the relevant reaction wheel speeds and excitations above the 8.3 Hz (500 rpm) minimum operating speed.

Each RWIA spring assembly consists of three primary flexile elements as shown schematically in figure 4. The parallel flexure/VEM load path allows shared strain energy, while the series flexure load path reduces the cutoff frequency and desensitizes the design to potentially large changes in shear stiffness of the VEM due to temperature fluctuations. Damping action in the isolator elements is obtained by shearing four small VEM pads. Material properties and dimensions were selected to yield a 5% modal damping ratio for the aforementioned isolator/reaction wheel system resonant frequencies at nominal operating temperature.

To allow the RWIA to withstand launch loads, a passive restraint system was included in the design of the RWIA spring elements. This restraint mechanism consists of a pin and clevis intersecting a post containing a Viton elastomer bumper

as shown in the schematic of figure 4. As the spring deflects, the bumper is engaged and axial load is diverted predominantly through the much stiffer post, thus preventing overload of the internal flexures.
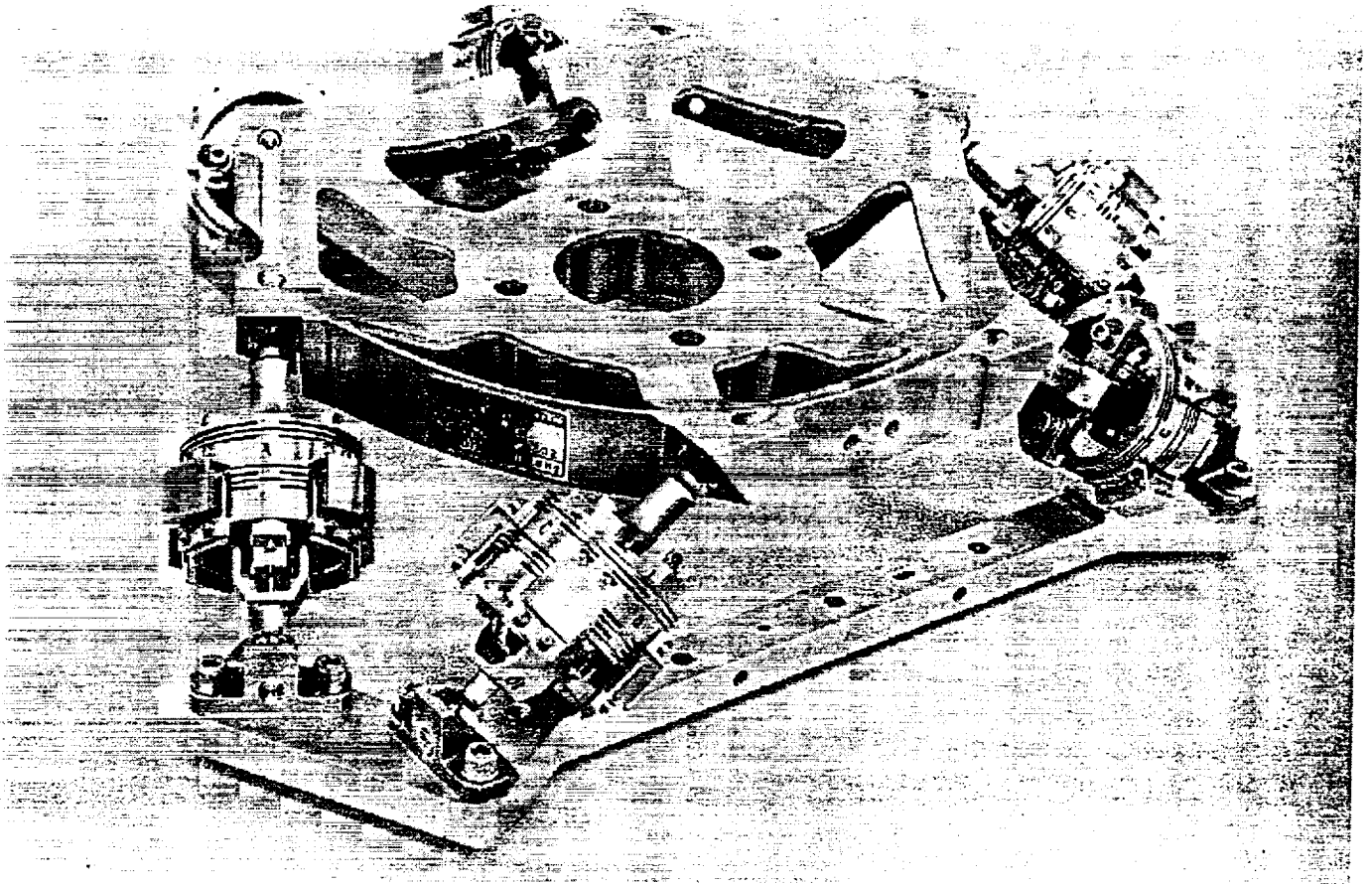

Figure 3: RWIA spring elements mated to the cradle and bottom bracket

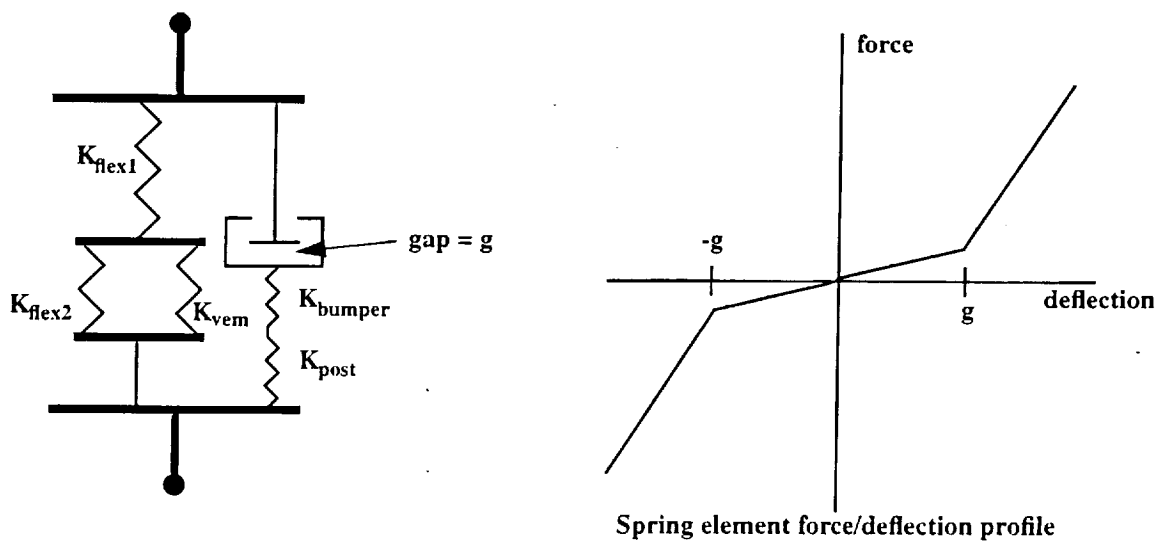Spring element force/deflection profile

Figure 4: Schematic representation of the RWIA spring elements, including force/deflection profile

Figure 5 contains two photographs that show the final configuration for two of the six RWA/RWIA units as attached to the spacecraft central cylinder. Visible in these photographs are the RWA units (the darker disc-like shape) attached to the cradle of the RWIAs. Also illustrated are the spring elements attached to the cradle and bottom bracket, which, in turn, is mated to the cylindrical bottom bracket mounting support. The mounting support was designed to withstand the launch loads of the cantilevered RWA/RWIA mass, and serves to interface the entire assembled unit to the spacecraft central cylinder. Each of the bottom bracket mounting supports was designed using an interface angle such that the momentum vectors of the six wheel constellation form a specified geometrical configuration.
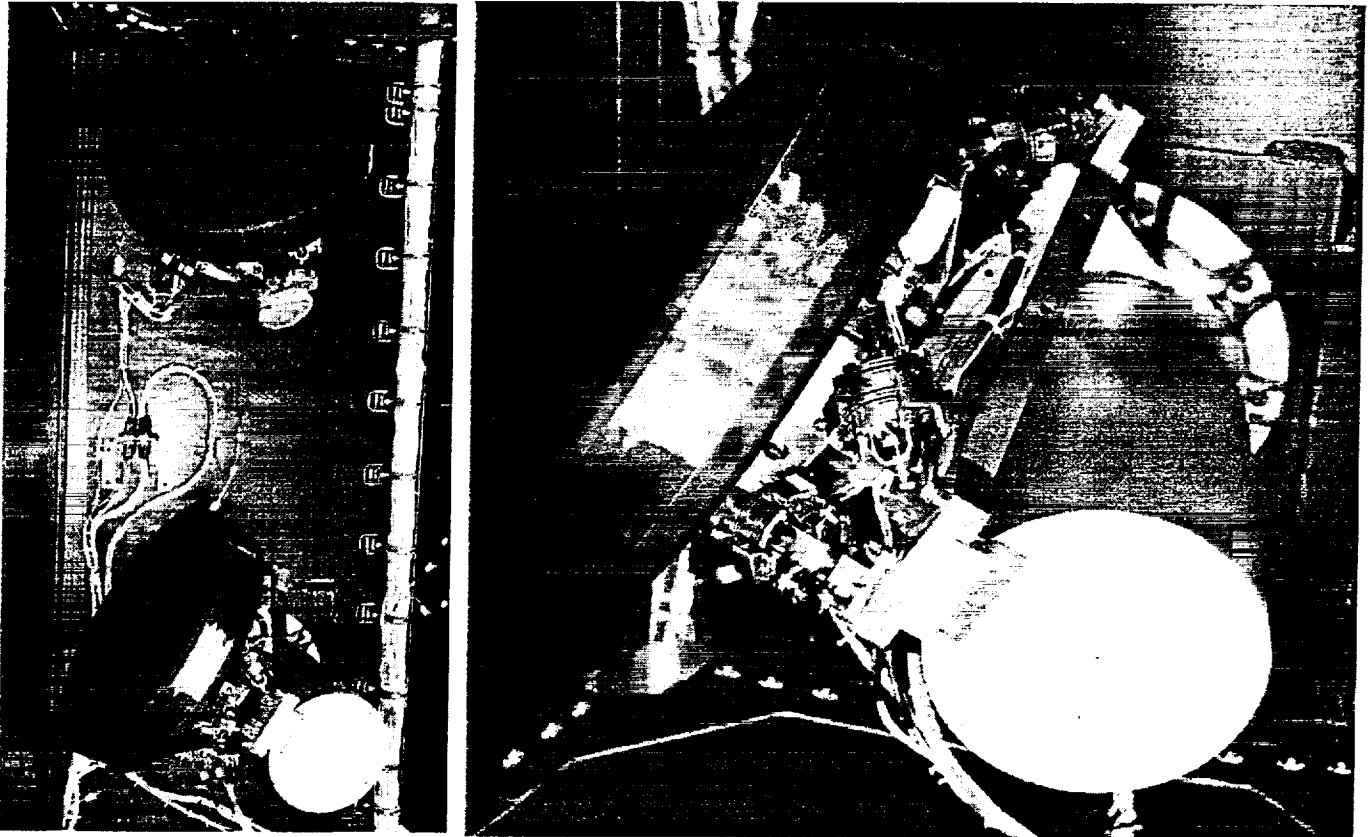

Figure 5: RWA/RWIA integrated configuration

4.0 IMAGE QUALITY REQUIREMENT

Due to the high sensitivity of the observatory optical train, passive isolation of reaction wheel sinusoidal disturbances was necessary as explained in the introduction. The following sections illustrate the flowdown of top level performance requirements (specifically the driving top level requirement) necessary for development of an equipment level specification that allows for a producible isolator design[1].

4.1 Requirement protocol

Figure 6 provides a graphic illustration of the documentation and analysis that link top level system performance requirements with RWIA equipment level performance requirements. The top level requirements are provided by NASA Marshall Space Flight Center (MSFC) via the level II Project Requirements Document (PRD). This document is then interpreted and published by TRW with MSFC concurrence as the Contract End Item (CEI) specification. These documents contain performance specifications for observatory pointing and imaging relevant to the determination of unit level RWIA equipment specifications for disturbance transmissibility. Specifically, the PRD and CEI specifications contain requirements for limitations on the effects of internal dynamic disturbances.

The CEI specification flows down observatory level requirements to spacecraft level requirements that are segregated by subsystems. The spacecraft subsystems specification flows down to the RWIA equipment specification that contains the key performance requirements on disturbance transmissibility across the RWIA.
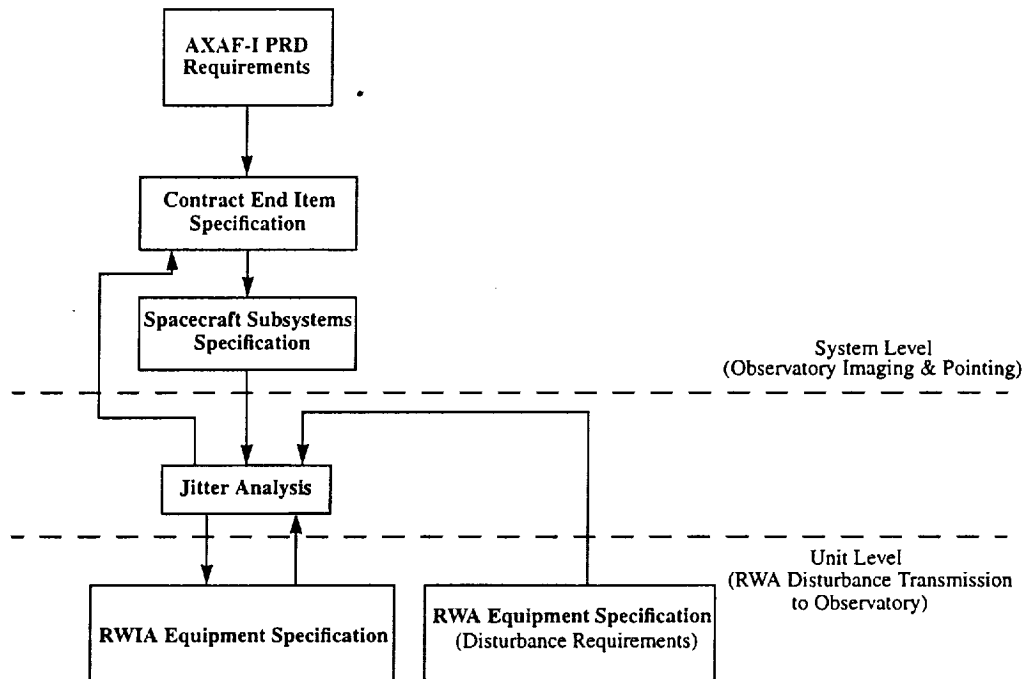
5

Figure 6: RWIA Key Performance Requirements Flowdown

4.2 System level to unit level requirements generation

The link between system level performance requirements on pointing and imaging and unit level performance requirements on transmissibility is made by analysis. The jitter analysis presented in the following two sections of this paper provides this link as illustrated in Figure 6. This analysis shows that the driving requirement (jitter induced image size growth due to distributed HRMA responses) is met by a minimum factor of 2.8. The driving requirement is defined as:

> *HRMA jitter shall contribute no greater than 0.229 arcseconds (11.2 μm) growth
> in the RMS diameter of the energy distribution at the telescope focal plane for a
> 0.277 KeV incident X-ray. The corresponding requirement for a 9.73 KeV
> incident X-ray is 0.275 arcseconds (13.4 μm).*

The jitter analysis assumes unit level specification values for the reaction wheel disturbances, and an analytical representation of the RWIA embedded in the observatory NASTRAN finite element model (FEM). This representation is combined with a momentum source representative of the RWA. This same representation is used to generate predictions of unit level transmissibility assuming a stationary reaction wheel mass (zero momentum source), and a fixed base. These assumptions are necessary to maintain consistency with the restrictive conditions of unit level testing for verification of RWIA requirements that preclude the use of an active RWA.

The margin of 2.8 determined by the jitter analysis is allocated to the analytical prediction for RWIA transmissibility consistent with unit level test conditions. The resultant transmissibility requirement is presented as the solid line in figures 7 through 9. The transmissibility is defined over a frequency range from 0 to 200 Hz and applies to five degrees of freedom. These five degrees of freedom include two orthogonal translations and two orthogonal rotations in a plane perpendicular to the RWA spin axis, and an axial translation aligned with the spin axis. In order to maintain pointing control system performance, the axial rotation d.o.f. is designed so that wheel control torques are not attenuated. A simplified stiffness requirement for axial rotation (M_z) is provided in the RWIA equipment specification for this purpose. Due to symmetry, definition of only three transmissibility curves is necessary, F_x and M_x (transverse force and moment), and F_z, force along the axial direction. The remaining rigid body degrees of freedom, F_y and M_y, are symmetrical to F_x and M_x, respectively.

## 4.3 Transmissibility frequency considerations

RWIA Engineering Model (EM) test results indicate some dispersion, but generally good correlation with the unit level analytical prediction for RWIA transmissibility as shown in figures 7-9. The margin of 2.8 used to loosen the

transmissibility requirement from the analytic prediction is insufficient from the standpoint of unit producibility at low frequency (< 20 Hz). The on-orbit jitter analysis, however, shows performance margins well in excess of 2.8 within this range. The worst case performance margin of 2.8 was initially applied uniformly across all frequencies due to the somewhat unpredictable movement of local isolator modal frequencies (from a fixed base unit test to a free-free on-orbit condition). Below 20 Hz the movement of isolator modal frequencies (clearly identified in the test data and analytic traces) is predictable, and insignificant. The RWIA modes were identified for each condition via strain energy analysis. Given this fact, low frequency system performance margin predicted by the jitter analysis may be mapped one for one (in terms of frequency) in allowing additional relaxation of the unit-level requirement.

4.4 RWIA modal frequency uncertainty

The RWIA transmissibility requirement is derived from the analytical prediction provided by the jitter analysis. It is clear in figures 7-9 that some dispersion in terms of frequency exists between EM test data derived transmissibility and the analytical prediction. Three factors account for this dispersion: 1) the variability of the VEM stiffness with input frequency (conservatively chosen to correspond with input frequencies below 10 Hz and modeled as a constant over frequency), 2) the analytical prediction assumes an infinitely stiff fixed base, but the RWIA test setup has a base frequency of approximately 500 Hz, and 3) the unit to unit variability in production of the RWIAs may contribute shifts in the RWIA modal frequencies of +/- 10%.

Given the aforementioned factors, the RWIA transmissibility is adjusted at high frequency (greater than 100 Hz) based on the EM test data. The EM test data was generated at TRW using a stinger input and a stationary reaction wheel mass simulator. This test data is a closer expectation of measured RWIA flight unit transmissibilities than the analytical prediction. Adjustments to the RWIA transmissibility requirement above 100 Hz based on EM test data are valid due to the high correlation between analytical model predictions and EM test data for frequencies less than 100 Hz. The final transmissibility requirements are presented in the figures.
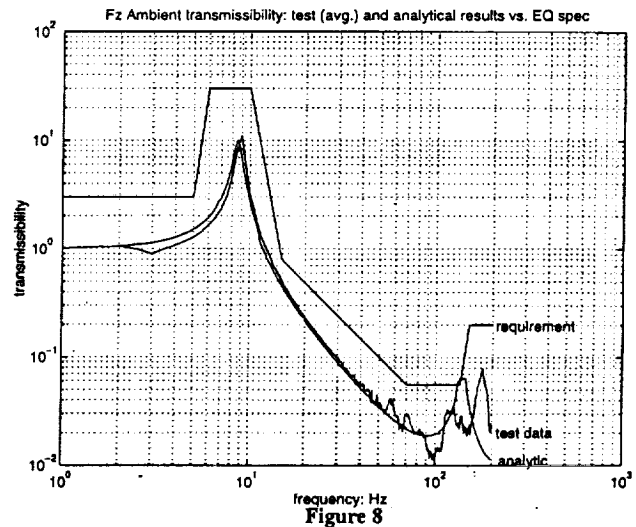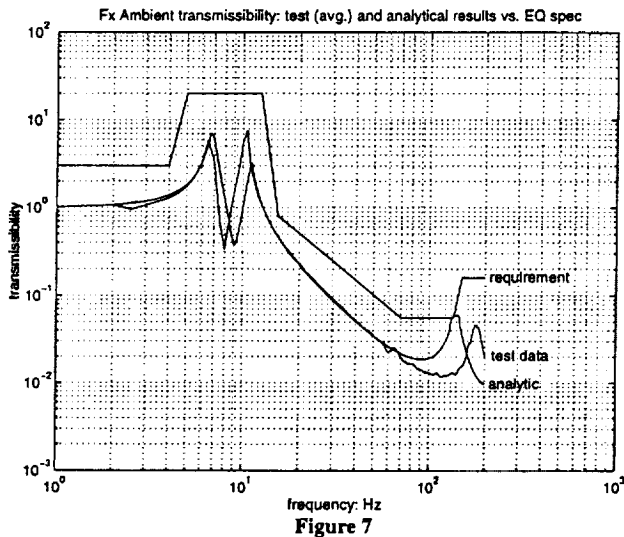
Figure 7

Figure 8

Figures 7-8: Unit-level transmissibilities - requirement, EM test data, and analytic predictions.
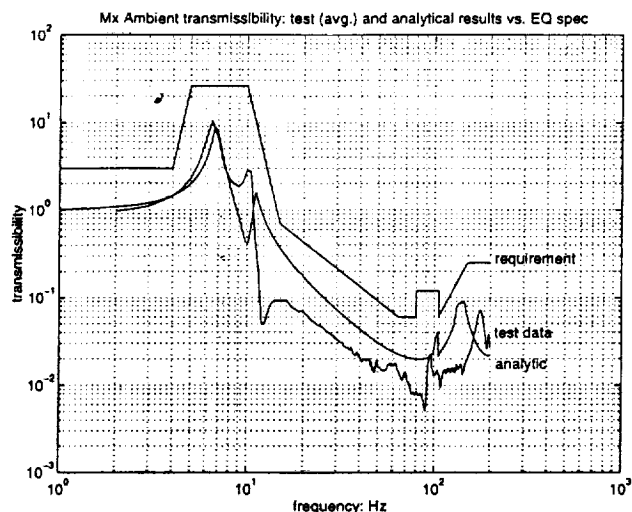
Figures 9: Unit-level transmissibilities - requirement, EM test data, and analytic predictions.

5.0 REACTION WHEEL JITTER DISTURBANCES

5.1 Jitter disturbance magnitudes

The only sources of significant spacecraft jitter for AXAF are disturbances from the reaction wheel assemblies. The three dominant reaction wheel disturbances are:

Static imbalance force disturbance

The static imbalance is an offset of the center of mass (CM) of the RWA rotor with the rotor spin axis, and results in a radial force rotating at the wheel frequency in a plane perpendicular to the rotor spin axis. The imbalance as a function of the wheel speed, ω, is determined from the specification by using the following equation,

$$S(\omega) = -3.78 \times 10^{-6}\omega + 0.0154 \quad \text{in-oz,} \tag{1}$$

where ω is the wheel spin rate in rad/s. Using this expression, the radial force generated by the imbalance is given as follows,

$$F_{S\_IMB}(\omega) = mr\omega^2 = \frac{mgr}{g}\omega^2 = \frac{S(\omega)}{g}\omega^2 \quad \text{lb,} \tag{2}$$

where m is the rotor mass, and r is the mass offset. Proper unit conversion yields the final expression for the static imbalance force in lb.

$$F_{S\_IMB}(\omega) = 1.619 \times 10^{-4}S(\omega)\omega^2 \quad \text{lb} \tag{3}$$

Dynamic imbalance torque disturbance

The dynamic imbalance is an angular offset of the RWA rotor principle axis with the rotor spin axis, and results in a radial torque rotating at the wheel frequency in a plane perpendicular to the rotor spin axis. The imbalance as a function of the wheel speed, ω, is determined from the specification by using the following equation,

$$D(\omega) = -5.95 \times 10^{-5}\omega + 0.1013 \quad \text{oz-in}^2, \tag{4}$$

where ω is again given in rad/s. Using this expression, the radial force generated by the imbalance is

8

given as follows,

$$T_{D\_IMB}(\omega) = (I_P - I_S)A\omega^2 = \frac{(I_P - I_S)Ag}{g}\omega^2 = \frac{D(\omega)}{g}\omega^2 \quad \text{ft-lb,} \tag{5}$$

where I_P and I_S are the moments of inertia about the principle and spin axes, respectively, and A is the angular offset between the two axes. Proper unit conversion yields the final expression for the dynamic imbalance torque in ft-lb.

$$T_{D\_IMB}(\omega) = 1.349 \times 10^{-5} D(\omega)\omega^2 \quad \text{ft-lb} \tag{6}$$

Axial force disturbance

In addition to the disturbances generated by the imbalances, oscillatory forces are generated in the direction of the wheel spin axis because of imperfections in the RWA bearings and bearing raceways. These forces are assumed to oscillate at the frequency of the wheel spin rate and have a magnitude increasing with the square of the spin rate. Under the assumption that the largest force occurs at the maximum NPM wheel speed of 4000 RPM, the magnitude is given by the following expression.

$$F_{AX}(\omega) = 2.563 \times 10^{-7} \omega^2 \quad \text{lb} \tag{7}$$

5.2 Use of wheel disturbances in jitter analysis

The analysis presented in the following sections involves determination of the X-ray image size response over a 0 to 150 Hz frequency range using the spacecraft NASTRAN finite element model (FEM). The response to RWA jitter disturbances in terms of image size at each of the FEM modal frequencies was generated for each of the six RWAs using the process shown schematically in figure 10. Within that process, fundamental, second harmonic (occurring at twice the frequency of the fundamental), and third harmonic (occurring at three times the frequency of the fundamental) disturbances are used to drive the FEM, resulting in estimates for the image size response as a function of modal frequency. Having determined the responses for each of the six RWAs, an RSS of the two largest is used to generate the final value for image size against which the mission requirement was compared. Note that the two largest responses are used to conservatively capture the minimal possibility that two of six wheels can operate in a speed synchronous condition during a typical scientific observation.

Several details worthy of discussion have been incorporated into this procedure.

1. The harmonic disturbances are assumed to be of a magnitude equal to one quarter of the fundamental disturbances at the wheel speed required for excitation of the mode under consideration. Teldix microvibration test data indicates that this is a sufficiently conservative approach; the data consistently indicate second and third harmonic disturbance magnitudes more than an order of magnitude smaller than the fundamentals.

2. For the three sets of disturbances (i.e. the fundamental, second harmonic, and third harmonic), the static and dynamic imbalance disturbance responses are added, and the result is RSS'd with the axial disturbance response. The justification for this approach lies in the results of a probabilistic study that concluded an RSS of all three responses is not adequately conservative given the constant-phase relationship between the static and dynamic imbalance disturbances of a given wheel.

3. The responses to the fundamental, second harmonic, and the third harmonic are RSS'd to form the total response for the wheel under consideration. In the preliminary analysis, only the response to the disturbance at the modal frequency was used in comparison against the requirement. It was felt that this was not a sufficiently conservative approach because it ignored the possibility that for a given modal frequency, one of the other disturbance sets could occur at a frequency near that of a different mode. In this case, the response could be significantly greater than that found by considering only the disturbance at the modal frequency being examined.

4. Above a frequency of 67 hz, which corresponds to a maximum on-orbit scientific mode RWA operational speed of 4000 rpm, the process assumes modal frequencies are being excited by higher harmonics of a wheel operating at either 1/2 or 1/3 of the modal frequency.

The next section addresses the method by which the disturbance forces and torques are used to determine the individual responses shown in the schematic of figure 10.
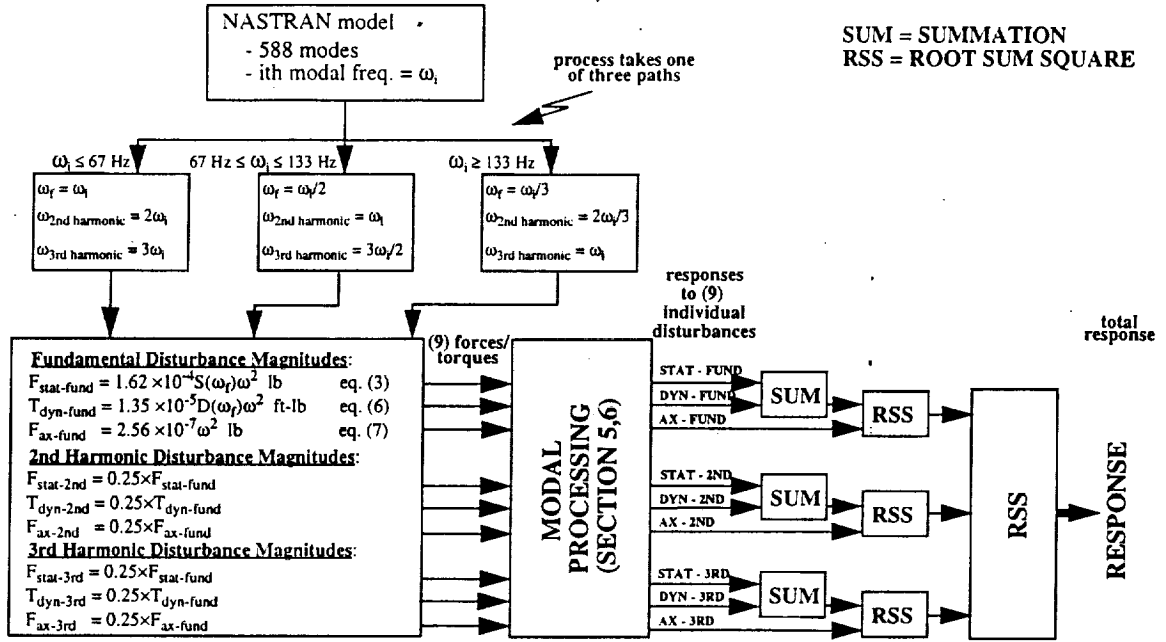
Figure 10: Schematic of process used to form a generic response to the disturbances arising from a single reaction wheel at a given modal frequency ω_i

6.0 SOLUTION FOR NODAL DISPLACEMENT IN RESPONSE TO RW JITTER

The response results given in the next section were found via solution to the complex system of differential equations formed using a representative NASTRAN FEM of the on-orbit AXAF observatory. In general, the FEM is used to form a decoupled system of equations driven by generalized forces found using the mode shapes at the location of any force/torque input to the system. Because of the decoupled nature of these modal differential equations, a solution for the modal coordinates may be easily found and used to compute the expected response in terms of translations or rotations at any node on the spacecraft for which the mode shapes are supplied. This is the exact approach used in the preliminary analysis, and served to produce an accurate estimate of the expected jitter responses. A brief reiteration of that method is given here.

As an example, consider the solution for the response in terms of a particular nodal translation/rotation to the static imbalance disturbance of a single wheel. The magnitude of the ith mode generalized force due to the static imbalance disturbance of the wheel rotating at ω_j is given by

$$Q_{ij} = F_{S\_IMB}(\omega_j)(\lambda_{ix}^2 + \lambda_{iy}^2)^{1/2}, \tag{8}$$

where λ_{ix} and λ_{iy} are the ith modal eigenvector translational components normal to each other, and in the plane perpendicular to the spin axis of the wheel, and $F_{S\_IMB}(\omega_j)$ is given by equation (3). Because of the rotational (i.e. sinusoidal) nature of the disturbance forces/torques, the time function representing the generalized force is defined as

$$Q_i(\omega_j) \equiv Q_{ij} \sin(\omega_j t). \tag{9}$$

The generalized coordinate, q_i, is then found via solution to the second order differential equation for the damped oscillator driven by this sinusoidal generalized input. Referring to the discussion above, note that the equation for the ith modal coordinate takes this form because of the decoupled nature the modal system,

$$\ddot{q}_i + 2\zeta_i\omega_i\dot{q}_i + \omega_i^2 q_i = Q_i(\omega_j), \tag{10}$$

10

where ζ_i and ω_i are the ith mode modal damping and frequency, respectively. The steady-state solution to this equation is given in the time domain as

$$q_i(t) = Q_{ij} d_i \sin(\omega_j t - \alpha_i), \quad \cdot \tag{11}$$

where

$$d_i = \left\{ (\omega_i^2 - \omega_j^2)^2 + (2\zeta_i \omega_i \omega_j)^2 \right\}^{-1/2} \tag{12}$$

$$\alpha_i = \operatorname{atan}\left(\frac{2\zeta_i \omega_i \omega_j}{\omega_i^2 - \omega_j^2} \right). \tag{13}$$

The time displacement or rotation of the node being considered is then found by summation of the modal coordinates scaled by ϕ_i, the ith modal slope in the desired direction.

$$\delta(t) = \sum_i \phi_i q_i(t) \tag{14}$$

In matrix form, the Laplace-transformed complex system of equations takes the following form.

$$\left[I_{nmode} \, s^2 + \left[2\zeta\omega \right]_{diag} s + \left[\omega^2 \right]_{diag} \right] \bar{q}(s) = \bar{Q} \tag{15}$$

where

I_{nmode} = the identity matrix of dimension nmode × nmode (nmode = number of modes)

$\left[2\zeta\omega \right]_{diag}$ = the diagonal damping matrix, with an (i,i) element = $2\zeta_i \omega_i$

$\left[\omega^2 \right]_{diag}$ = the diagonal normalized stiffness matrix, with (i,i) element = ω_i^2

$\bar{q}(s)$ = the nmode-vector of modal coordinates

$\bar{Q}$ = the nmode-vector of modal generalized forces

Because of two effects included to improve the fidelity of this approach, the uncoupled system of equations represented by (15), for which the solution is given in (11) through (13), have become coupled. These two effects are gyroscopic torques imparted on the isolator due to the spinning reaction wheel, and the damping caused by viscoelastic material (VEM) used in the isolator spring assemblies. Both of these effects couple the modes of the isolator, causing inversion of the complex matrix similar to that on the left hand side of equation (15) to be required for solution of the modal coordinates.

The effect of the gyroscopic torques was treated in a similar manner to a previous TRW jitter analysis, in which the dynamics of the gyroscopic motion were incorporated into the structure of the modal equations given by (15). In order to understand this treatment, it is first necessary to recognize that equation (15) is the result of the eigenvalue solution to the system of equations for the spacecraft "lumped mass" model to which modal damping is added following the orthonormalization process. This process begins with the undamped lumped mass system of equations given by

$$M\ddot{y} + Ky = F, \tag{16}$$

where

M = the system mass matrix

K = the system stiffness matrix

F = the vector of applied forces/torques

y = the vector of system states

Using a matrix representation for the cross product operation, addition of the gyroscopic term due to the wheel angular momentum, H_w, yields the following form for the component of equation (16) that corresponds to the rotational motion of a given RWA/RWIA system.

$$I_{sys}\ddot{\theta} + H\dot{\theta} + K_{rwia}\theta = F(\omega_w),$$ (17)

where

$$H = \begin{bmatrix} 0 & H_w & 0 \\ -H_w & 0 & 0 \\ 0 & 0 & 0 \end{bmatrix}$$

($H_w = I_w\omega_w$, the RWA rotor angular momentum)

I_{sys} = the RWA/RWIA inertia tensor

K_{rwia} = the rotational spring forces due to the RWIA

$F(\omega_w)$ = the 3-vector sum of RWA disturbance torques

It can be seen that when the gyroscopic term due to the jth RWA is added to the entire lumped mass system of equations, and the result is transformed using the eigenvector decomposition of the $K^{-1}M$ matrix in the original equation, the following result for the modal system is achieved.

$$\left[\left[I_{nmode}\right]s^2 + \left[2\zeta\omega\right]_{diag}s + \Phi_{RWA_j}{}^T H\Phi_{RWA_j}s + \left[\omega^2\right]_{diag}\right]\bar{q}(s) = \bar{Q}$$ (18)

where

Φ_{RWA_j} = the matrix of rotational mode shapes corresponding to the jth RWA

Upon solution of the modal coordinate vector using equation (18), the gyroscopic effect of the jth RWA is, therefore, captured via summation of the RWA rotational components from all of the system modes following modification by matrix H.

The second additional effect captured in the current analysis that serves to further couple the modal system of equations is the damping of the VEM material in the RWIA spring assemblies. This effect was modeled in the NASTRAN solution by inclusion of a dashpot across each of the 24 VEM components in the six RWIA assemblies. The result of that approach is the formation of a complex stiffness matrix that can be included directly in the system of equation in (18) to form the final result for the full modal system of equations.

$$\left[\left[I_{nmode}\right]s^2 + \left[2\zeta\omega\right]_{diag}s + \Phi_{RWA_j}{}^T H\Phi_{RWA_j}s + \left[\omega^2\right]_{diag} + iK_4\right]\bar{q}(s) = \bar{Q}$$ (19)

where

K_4 = the NASTRAN-supplied complex stiffness matrix

Having formed the full modal system of equations, the solution for the complex modal vector $\bar{q}$ under the influence of rotational gyroscopic coupling from the jth RWA can be found via inversion of the left-hand-side (LHS) matrix and multiplication by the complex generalized force vector $\bar{Q}$.

·As an example, consider again a generic response to the static imbalance force from a given RWA rotating at a rate ω_j. Given the sinusoidal nature of the disturbance, the ith component of the resultant generalized force due to the static imbalance can be represented in complex form using the magnitude of the disturbance force given by equation (3).

$$Q_i(\omega_j) = F_{Simb}(\omega_j)(\lambda_{ix}^2 + \lambda_{iy}^2)^{1/2}(1 + i)$$ (20)

Using this equation to form the entire vector of modal generalized forces, the solution for the modal coordinate is simply found via the LHS complex matrix inversion described above. The final step in the generation of the response proceeds exactly as in the preliminary analysis using equation (14), with substitution of the complex representation for the ith modal coordinate.

$$\delta = \sum_i \phi_i q_i$$ (21)

Computation of the magnitude of the complex response, δ, then yields the result for the magnitude of the sinusoidal time response for the displacement (angular or translational) in the direction specified by the mode shapes ϕ_i. Note that the responses due to the dynamic imbalance and axial force disturbances are found in the same manner, but with the appropriate form for equation (20).

Given the fairly involved computational process describe above, a summary is in order.

<u>Summary for the solution to a nodal displacement in response to RWA jitter</u>:

1.   Form the set of nine jitter disturbances using the process described in the first three steps of figure 10. The force and torque magnitudes are formed as a function of the wheel rate, which is determined from the modal frequency under consideration.

2.   Form the nine generalized force vectors using equation (20), where ω_j is equal to the frequency of the corresponding disturbance as shown in figure 10.

3.   For each wheel, construct the LHS matrix of equation (19) for each of the three input disturbance frequencies. These matrices are formed using the wheel rotational rate in the angular momentum matrix and $s = i\omega_{dist}$, where ω_{dist}, is the disturbance frequency. Note here that the 0.2% damping has again been assumed for all modes of the system except those due to propellant slosh, for which 0.5% was used.

3.   For each wheel at each of the three disturbance frequencies, invert the LHS matrix and multiply by the corresponding generalized force vectors to solve for the nine complex modal coordinate vectors.

4.   For each wheel, use the modal coordinate solution from step 3 to solve for the displacement responses to the nine individual RWA disturbances according to equation (21).

5.   From the nine responses for each wheel, compute the total wheel response as shown in figure 10. That is, sum the three sets of static and dynamic imbalance disturbance responses and RSS this result with the corresponding response to the axial disturbance. RSS those three results to form the total response of each wheel to the RWA jitter disturbances.

6.   From the set of six total wheel responses, RSS the two largest to determine the nodal displacement of interest.

7.0 HRMA IMAGE SIZE GROWTH

The X-ray image at the focal plane of the telescope can be blurred by the effects of jitter disturbances on the HRMA surfaces. Specifically, jitter causes vibration of the mirror surfaces in well-defined shapes which can be modeled for the purpose of quantifying the increase in the image size at the FPSI detectors from that of an ideal (point) image. The entire process by which this is accomplished is discussed in this section, with results for image size as a function of jitter frequency being given in closing.

7.1 Image Size Determination Methodology

The method of Genberg[2,3] from EKC has been used to generate the coefficients of Fourier-Legendre (FL) optical element surface shape approximation polynomials based on a linear combination of the modal displacements of the HRMA nodes in the spacecraft NASTRAN model. The solution for the approximation function coefficients is based on a least squares fit of the HRMA mode shapes to the shape given by the FL surface function, and is encoded into the NASTRAN model in the form of multi-point constraint (MPC) relations. These NASTRAN encoded MPC relations are used to generate FL coefficients for a unit generalized modal coordinate, herein termed the normalized coefficients.

Determination of the HRMA image size at the focal plane via use of the normalized FL coefficients is accomplished by the analytical tracing of incident rays through the telescope system by a workstation-based program written by the author. This program, KPTRACE, accepts the FL coefficients as input, models the HRMA geometrical structure, and uses the result of the trace of 2000 uniformly distributed rays through the telescope apertures to determine the expected image size for both the upper and lower bounds on the energy of the incident rays. Incident ray energy effect on the image size is accounted for by weighting the energy of the ray at the focal plane based on the HRMA mirror pair upon which it was incident. For example, a high energy ray transmits only 1% of the incident energy to the focal plane if it is reflected through the telescope system by the P1-H1 mirror pair (largest diameter nested pair), whereas it retains 95% of the incident energy if it passes through the telescope system by reflection off the P6-H6 pair (the smallest diameter nested pair). In this way, the ray locations at the focal plane are weighted by energy so that the image centroid and size are given in terms of the energy of the ray photons at the plane of the science instrument detectors. Therefore, given a set of FL surface descriptor coefficients, the centroid of the image in terms of energy and the root mean square (RMS) distribution of that energy about the centroid are determined using the KPTRACE ray tracing program. It is noted that a full validation of the KPTRACE results for image shape and size was accomplished via exact agreement of those results for several test cases with those of an independent ray tracing program (Quicktrace) supplied by EKC.

The following method was used to determine the image sizes based on the solution to the modal coordinates described in the previous section. Since this method considers the image growth contribution of all system modes, it has been termed the "full mode" solution; the differentiation is made here because the original simplified method discussed in the introduction found the image size growth at each modal frequency in response to only the resonant mode.

The method of Genberg determines the coefficients of the FL polynomials using a linear combination of the modal displacements of the HRMA nodes in the NASTRAN model. Because of this, it is possible to factor the modal coordinate term out of the 15 coefficients used to approximate the shape of each of the eight mirror surfaces at a given disturbance frequency. (Note that it is this feature of the FL coefficients that allows generation using the MPC relations and a unit generalized modal coordinate.) Assuming the use of n HRMA nodal displacements, this factorization can be shown as follows for the mth coefficient out of the 15 used for each mirror at the ith disturbance frequency.

$$C_{im}(t) = \sum_{l=1}^{n} \beta_{iml}\delta_{il}(t) = q_i(t)\sum_{l=1}^{n} \beta_{iml}\phi_{il} \qquad (22)$$

Continuing, it is necessary to understand that the FL polynomials give the displacement of the n HRMA nodes in the direction normal to the undeformed surface via a linear combination of the 15 coefficients. That is,

$$\delta_i(t) = \sum_{m=1}^{15} \gamma_m C_{im}(t), \qquad (23)$$

where the $\delta_i(t)$ is now the displacement of a generalized HRMA node in the direction normal to the undeformed surface caused by the ith mode. Note that the γ_m are dependent (geometrically) only on the location of the node, and are, therefore, invariant with frequency for a given node, as shown.

Substitution of (22) into (23) yields the following expression for this modal displacement,

$$\delta_i(t) = q_i(t)\sum_{m=1}^{15} \gamma_m \sum_{l=1}^{n} \beta_{iml}\phi_{il} \qquad (24)$$

where ϕ_{il} is the magnitude of translational component of the ith modal eigenvector in the direction normal to the undeformed surface at the lth HRMA node.

Since the total normal displacement of the surface at the HRMA node under consideration is found by the summation of the modal displacements, it is possible to write the following expression for the total displacement.

$$\delta(t) = \sum_i \delta_i(t) = \sum_{m=1}^{15} \gamma_m \sum_i q_i(t) \sum_{l=1}^{n} \beta_{iml}\phi_{il} \qquad (25)$$

Finally, substitution of (22) into (25) yields

$$\delta(t) = \sum_{m=1}^{15} \gamma_m \sum_i q_i(t)C_{im}^{\perp}, \qquad (26)$$

where $C_{im}^{\perp}$ are the normalized FL coefficients supplied by the NASTRAN MPC relations using unit generalized modal coordinates.

Hence, a form for the full-mode displacement of the HRMA nodes as a function of the normalized coefficients and the modal coordinates has been found. Specifically, these coefficients are given by a full-mode equivalent to the modal FL polynomials, with the full-mode coefficients being given by the following expression.

$$C_m(t) = \sum_i q_i(t)C_{im}^{\perp}, \qquad (27)$$

where the modal coordinates, q_i, are found by the solution of the previous section.

14

The final step in this methodology is the determination of the spatial RMS image size resulting from the use of the above coefficients. Note that the mapping from coefficient set to image size is only determinable via use of the KPTRACE ray tracing program. Since the full-mode versions of the FL coefficients vary nonlinearly with time (i.e. each ith mode coefficient set varies sinusoidally out of phase), it is necessary to compute the spatial RMS for the image size at times uniformly distributed through an entire cycle of the jth disturbance frequency. The final result for the spatial RMS image size is then given as the mean of the individual RMS image sizes. Mathematically, this is represented as follows.

The RMS image size is computed for each of 24 sets of full-mode coefficients, where the rth set at frequency ω_j is

$$\{C_r\} = \sum_i q_i(t)\left\{C_i^{\perp}\right\} = \sum_i \|q_i\| \sin\left(\frac{2\pi r}{24} - \alpha_i\right)\left\{C_i^{\perp}\right\}, \tag{28}$$

where α_i, is the phase of the ith complex modal coordinate generated using equations (19) and (20), and q_i is the magnitude of that modal coordinate.

Because of the computational burden of the ray-tracing software, it is not particularly desirable to compute the nine individual responses in terms of image size from the solution to the nine sets of modal coordinates given in the previous section. As a result, a slightly simplified approach has been used to compute the image size response.[†] Instead of combining the nine responses in the sum/RSS method described by the schematic of figure 10, the modal coordinate vectors are first combined in the same fashion at each of the three disturbance frequencies (i.e. the fundamental and two higher harmonic frequencies) to form three modal coordinate vectors for each wheel. A final set of modal coordinate vectors corresponding to the three disturbance frequencies is then found by RSSing the modal coordinate vectors of the two wheels with the largest magnitude of the component corresponding to the modal frequency under consideration. Note that since the RSS procedure eliminates the modal phase information, the phase for each ith modal component is determined using the assumed modal damping.

$$\alpha_i = \text{atan}\left(\frac{2\zeta_i \omega_i \omega_{dist}}{\omega_i^2 - \omega_{dist}^2}\right). \tag{29}$$

Three responses in terms of the image size are then computed using the ray-tracing software, with the results being RSS'd to form the total response at each modal frequency.

The results of the procedure described above for both the low and high energy bounds on the image size requirement spectrum are plotted against the system level requirements of 11.2 μm and 13.4 μm in figure 11. The reader should keep in mind that the variant along the abscissae of the plots shown in figure 11 is the assumed frequency of the primary disturbance driving the system. This primary disturbance is a fundamental, second harmonic, or third harmonic of a wheel rotating at the speed required to generate disturbances occurring at exactly the modal frequencies specified by the spacecraft FEM. As discussed in section 5, the two modeled disturbances other than the primary are also included in the determination of the responses at the primary disturbance frequencies, but have not been referenced in the plots of figure 11. Note that the wheel speed required to generate disturbances at the FEM modal frequencies could have been used (for those disturbances above the 67 Hz RWA operational speed) as the abscissa variant. As opposed to the chosen method, however, use of the wheel speed would have resulted in a "folding" of the data into a 0 - 67 Hz range, thus eliminating valuable information about the behavior of the system.

It can be seen that the low energy case contains the largest magnitude maximum response, with the minimum margin factor of 2.8 occurring at a modal frequency of roughly 132 Hz. The high energy X-ray case exhibits a minimum margin factor of 8.2 at a modal frequency of 19.7 Hz. Given the difficulty involved with physically characterizing the 132 Hz mode responsible for the maximum response of the high energy bound, it will only be said here that the HRMA has strong participation at that frequency. It can be said with relative certainty, however, that the 19.7 Hz frequency at which the maximum response for the low energy bound occurs is very nearly the frequency of a primary mode of the spacecraft central cylinder.

---

† The determination of the other jitter responses (i.e. other than X-ray image size growth) not discussed in this paper used the specific process shown in figure 2.

The next section contains the results for the isolated system image size response compared to those generated using a spacecraft FEM that excludes the RWIA units.
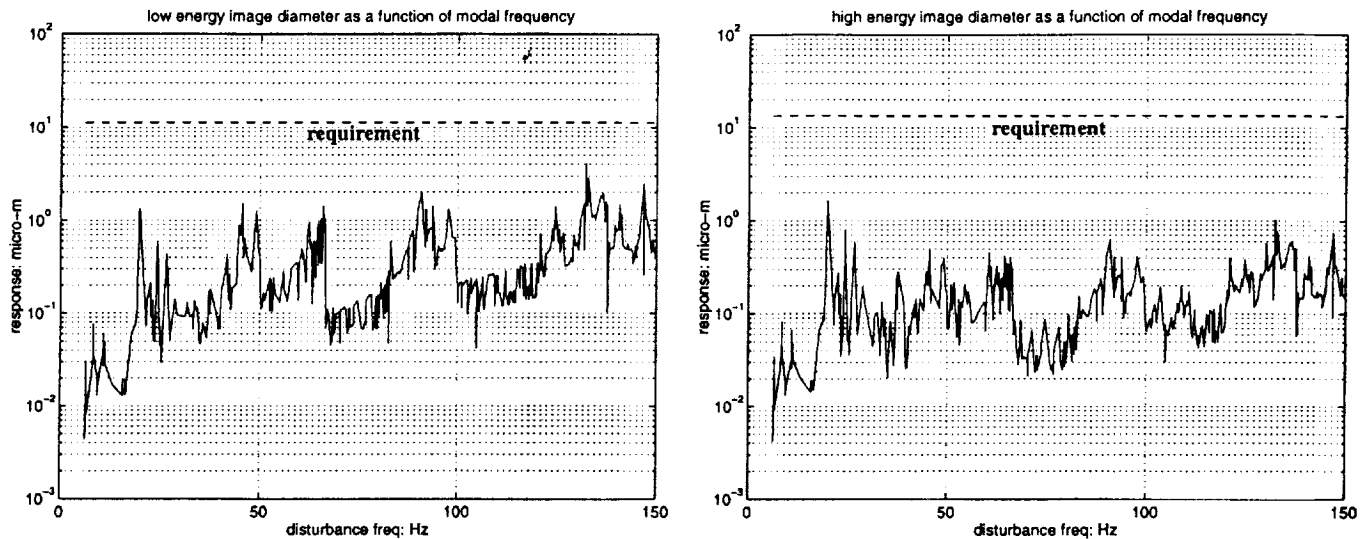

Figure 11: Results for X-ray image energy diameter found using the methods of sections 6,7

7.2 Comparison of isolated and nonisolated image size responses

To facilitate evaluation of the RWIA effectiveness, it is helpful to compare results for the isolated system image size response to those found using a spacecraft FEM that does not contain the RWIA units. In fact, the image size response analysis performed on the original system serves this purpose well. As discussed in the introduction, this analysis was performed for the purpose of quantifying the original system (i.e. prior to the addition of the RWIAs) response to RWA disturbances that led to the initiation of the isolator design.

Without the modal coupling effects resulting from the inclusion of the RWIA, the straightforward process outlined in section 6 equations 8 through 13 can be used to determine modal coordinate vectors generated by the three types of RWA jitter disturbances. These results can then be used directly in the procedure outlined in section 7 to generate estimates for the non-isolated image size responses. Results for X-ray image size found for the non-isolated system in exactly this fashion are plotted against the isolated system results in figure 12. It is noted that two facets of the final analytical method included to increase the conservativeness of the results were not included in the original analysis. Firstly, the image size responses to the three jitter disturbances were all RSS'd in the original analysis. This is in contrast to the final methodology shown in figure 10 that indicates the static and dynamic disturbance responses were added. Secondly, the original analysis only considered the presence of a fundamental disturbance at the modal frequencies, thus ignoring any contributions from higher harmonic disturbances as indicated in the methodology of figure 10.

The effectiveness of the isolation system is clearly demonstrated by the results shown in figure 12. While the non-isolated system clearly shows violations of the respective image size requirements for both bounds of the X-ray energy, the isolated system falls within a minimum factor of 2.8 from the requirement over all disturbance frequencies. However drastic the differences in the data shown in the plots of figure 12, the reader should take care in drawing too quantified of a conclusion from the results. Because of differences in the FEMs used to determine the results, behavior such as shifts in frequency of system zeroes and poles and changes in modal characteristics can occur, thus preventing comparison of the results on a frequency-by-frequency basis. Taken in a qualitative sense, however, the data strongly demonstrates not only the necessity for the isolator system, but also the effectiveness of the final design in terms of system level performance.
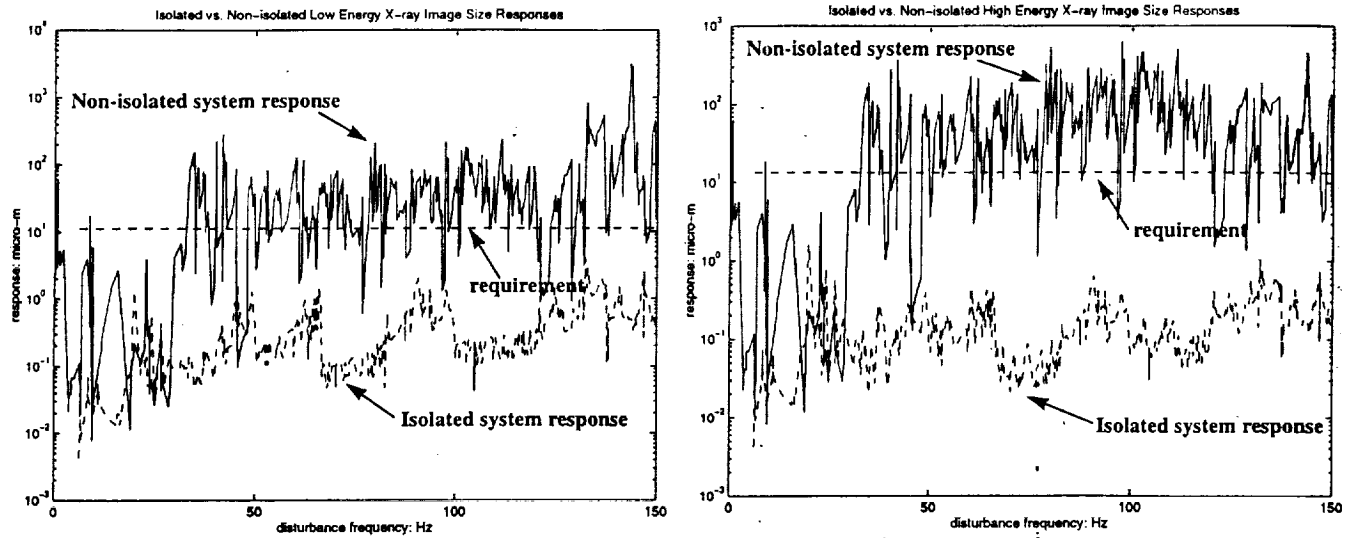
16

Figure 12: Comparison of the isolated system image size responses to that of the non-isolated system

8.0 CLOSING REMARKS

An innovative passive reaction wheel isolation mechanism has been designed to allow the used of conventional reaction wheels on a high resolution space based imaging system. The method by which the isolation system was designed and constructed involved complex manipulations of various requirements, test data, and analytical results. This paper serves as documentation of this approach in addition to providing details of the analytical methodology used to verify compliance with system level image quality requirements.

9.0 REFERENCES

1. Schauwecker, C. J., et al, "Imaging Pointing Control and Aspect Determination System for the NASA Advanced X-Ray Astrophysics Facility," *Proc. of the Annual AAS Rocky Mountain Guidance and Control Conference*, AAS **97-04**, pp. 233-249, 1997.

2. Genberg, V., "Optimum Design of a Lightweight Telescope," *Proc. of the MCS/NASTRAN Users Conference*, May, 1995.

3. Genberg, V., "Optical Surface Evaluation," *SPIE Cambridge Symposium on Structural Mechanics of Optical Systems*, 07-08 November, 1983.